Electronic and vibrational properties of PbI$_2$: From bulk to monolayer

M. Yagmurcukardes,[1,*] F. M. Peeters,[1] and H. Sahin[2,3]

[1]*Department of Physics, University of Antwerp, Groenenborgerlaan 171, B-2020 Antwerp, Belgium*
[2]*ICTP-ECAR Eurasian Center for Advanced Research, Izmir Institute of Technology, 35430, Izmir, Turkey*
[3]*Department of Photonics, Izmir Institute of Technology, 35430, Izmir, Turkey*

Using first-principles calculations, we study the dependence of the electronic and vibrational properties of multilayered PbI$_2$ crystals on the number of layers and focus on the electronic-band structure and the Raman spectrum. Electronic-band structure calculations reveal that the direct or indirect semiconducting behavior of PbI$_2$ is strongly influenced by the number of layers. We find that at 3L thickness there is a direct-to-indirect band gap transition (from bulk-to-monolayer). It is shown that in the Raman spectrum two prominent peaks, A_{1g} and E_g, exhibit phonon hardening with an increasing number of layers due to the interlayer van der Waals interaction. Moreover, the Raman activity of the A_{1g} mode significantly increases with an increasing number of layers due to the enhanced out-of-plane dielectric constant in the few-layer case. We further characterize rigid-layer vibrations of low-frequency interlayer shear (C) and breathing (LB) modes in few-layer PbI$_2$. A reduced monoatomic (linear) chain model (LCM) provides a fairly accurate picture of the number of layers dependence of the low-frequency modes and it is shown also to be a powerful tool to study the interlayer coupling strength in layered PbI$_2$.

I. INTRODUCTION

Over the past decade, successful synthesis of graphene [1,2] led to an enormous interest in the field of two-dimensional (2D) materials. However, the lack of a band gap in graphene restricted its applications and a search for other 2D materials with a suitable band gap became necessary. With this respect, many other 2D monolayer materials such as silicene [3,4], germanene [3], group III-V binary compounds (*h*-BN, *h*-AlN) [5–9], and transition-metal dichalcogenides (TMDs) [10–17] were successfully synthesized. Recently a post-transition metal iodide PbI$_2$ was added to the library of 2D monolayer materials [18].

Lead iodide (PbI$_2$) is a typical layered van der Waals (vdW) crystal in its bulk form which crystallizes in the well-known 1T phase. The PbI$_2$ units are also known to form lead halide perovskites which were recently investigated [19,20]. Its bulk crystal is composed of covalently bonded I-Pb-I repeating layers that interact weakly with vdW forces [21–25]. The bulk crystal of PbI$_2$ was demonstrated to be a good semiconductor for photoluminescence, electroluminescence, and nonlinear optical field applications [26,27]. In addition, thickness-dependent optoelectronic properties of PbI$_2$ is another important feature of the material. Toulouse *et al.* found theoretically that the electronic-band structure of PbI$_2$ exhibits a shift from a direct gap with 2.38 eV to an indirect-gap semiconductor with 2.5 eV when its thickness is thinned down to bilayer or monolayer [21]. In another study, Zhou *et al.* investigated the structural stability and strain-dependent electronic properties of monolayer PbI$_2$ and showed that the band gap of the material is tunable under biaxial strain in a wide energy

range of 1–3 eV [28]. Wang *et al.* confirmed experimentally the thickness- and strain-dependent photoluminescence properties of PbI$_2$ [29] and reported that thickness-dependent vdW epitaxial strain can be significant and influences substantially the photoluminescence properties of PbI$_2$. Very recently, Zhong *et al.* successfully synthesized large scale monolayer and few-layer PbI$_2$ with high crystallinity using the physical vapor deposition (PVD) method [18] and using photoluminescence measurements showed direct-gap to indirect-gap transition in PbI$_2$ when going from bulk to monolayer.

One of the most common techniques for the characterization of a material is Raman spectroscopy [30] which gives information about the structural phase of the material by monitoring the characteristic vibrational energy levels of the sample. Raman measurement can give information about the substrate-free number of layers identification of layered materials [31–33], the strength of the interlayer coupling in layered materials [33,34], and interface coupling in vdW heterostructures [35,36]. Absolute and relative activities of the Raman peaks lead to the determination of different phase distributions in a material [37–39]. Raman spectroscopy can also give information about the electronic structure, thickness, and can be used to probe strain, stability, stoichiometry, and stacking orders of 2D materials [40].

The PbI$_2$ crystal is known as a good semiconductor for photoluminescence, electroluminescence, and nonlinear optical field applications which is also known to possess important thickness-dependent optoelectronic properties. The thickness-dependent electronic properties of PbI$_2$ were already investigated by means of photoluminescence measurements and *ab initio* calculations. Here we aim to study the number of layer dependency of the electronic-band structure of PbI$_2$ and explain the physical origin of the indirect-to-direct band gap transition. In addition, we investigate the layer-dependent

*Mehmet.Yagmurcukardes@uantwerpen.be

085431-1

vibrational properties of PbI_2 in terms of high-frequency prominent optical peaks and low-frequency interlayer shear (C) and breathing (LB) modes in order to get information about the layer-layer interaction in few-layer PbI_2.

The paper is organized as follows: Details of the computational methodology and Raman scattering theory are given in Sec. II. The evolution of electronic-band structure with the number of layers is discussed in Sec. III A. In Secs. III B 1 and III B 2 the evolution of the Raman spectrum of PbI_2 from bulk to monolayer is discussed in terms of the peak frequencies and Raman activities of high-frequency optical and low frequency interlayer shear and breathing modes, respectively.

II. COMPUTATIONAL METHODOLOGY

To investigate the structural, electronic, and vibrational properties of PbI_2 crystals, first-principle calculations were performed in the framework of density functional theory (DFT) as implemented in the Vienna *ab initio* simulation package (VASP) [41,42]. The Perdew-Burke-Ernzerhof (PBE) [43] form of generalized gradient approximation (GGA) was adopted to describe electron exchange and correlation. The van der Waals (vdW) correction to the GGA functional was included by using the DFT-D2 method of Grimme [44]. The electronic-band structures were calculated with the inclusion of spin-orbit coupling (SOC) on top of the GGA and Heyd-Scuseria-Ernzerhof (HSE) [45] screened-nonlocal-exchange functional of the generalized Kohn-Sham scheme, respectively. The charge transfer in the system was determined by the Bader technique [46].

The kinetic energy cutoff for plane-wave expansion was set to 500 eV and the energy was minimized until its variation in the following steps became less than 10^{-8} eV. The Gaussian smearing method was employed for the total energy calculations. The width of the smearing was chosen to be 0.05 eV. Total Hellmann-Feynman forces were taken to be 10^{-7} eV/Å for the structural optimization. $18 \times 18 \times 1$ Γ centered k-point samplings were used in the primitive unit cells. To avoid interaction between the neighboring layers, the calculations were implemented with a vacuum space of 25 Å.

The phononic properties of PbI_2 crystals were calculated in terms of the off-resonant Raman activities of the phonon modes at the Γ point. For this purpose, the zone-centered vibrational phonon modes were calculated using the finite-difference method as implemented in VASP. Each atom in the primitive unit cell was initially distorted by 0.01 Å and the corresponding dynamical matrix was constructed. Then, the vibrational modes were determined by a direct diagonalization of the dynamical matrix. The kinetic energy cutoff for plane-wave expansion was increased to 800 eV with a k-point set of $24 \times 24 \times 1$ in the case of Raman calculations. The k-point set and kinetic energy cutoff were systematically increased step by step until convergence for the frequencies of acoustic modes was reached (0.0 cm^{-1} for each acoustic mode at the Γ point). Once the accurate phonon mode frequencies were obtained at the Γ point, the change of the macroscopic dielectric tensor was calculated with respect to each vibrational mode to get the corresponding Raman activities [47].

In a Raman scattering experiment, the sample is exposed to light and instantly scattered photons are collected.

The dispersion of the collected photons with respect to a shift in frequency gives the Raman spectrum. In Raman theory, the inelastically scattered photon originates from the oscillating dipoles of the crystal corresponding to the Raman active vibrational modes.

The treatment of Raman activities is based on Placzek's classical theory of polarizability [48]. According to the Placzek approximation, the activity of a Raman active phonon mode is proportional to $|\hat{e}_s R \hat{e}_i|^2$ where $\hat{e}_s$ and $\hat{e}_i$ stand for the polarization vectors of scattered radiation and incident light, respectively. R is a 3×3, second rank tensor known as the Raman tensor whose elements are derivatives of polarizability of the material with respect to the phonon normal modes,

$$R = \begin{bmatrix} \frac{\partial \alpha_{11}}{\partial Q_k} & \frac{\partial \alpha_{12}}{\partial Q_k} & \frac{\partial \alpha_{13}}{\partial Q_k} \\ \frac{\partial \alpha_{21}}{\partial Q_k} & \frac{\partial \alpha_{22}}{\partial Q_k} & \frac{\partial \alpha_{23}}{\partial Q_k} \\ \frac{\partial \alpha_{31}}{\partial Q_k} & \frac{\partial \alpha_{32}}{\partial Q_k} & \frac{\partial \alpha_{33}}{\partial Q_k} \end{bmatrix}, \tag{1}$$

where Q_k is the normal mode describing the whole motion of individual atoms participating to the kth vibrational phonon mode while α_{ij} is the polarizability tensor of the material. The term $|\hat{e}_s R \hat{e}_i|^2$ is called the Raman activity which is calculated from the change of polarizability. For a backscattering experimental geometry the total Raman activity is represented in terms of Raman invariants given by

$$\tilde{\alpha}_s \equiv \frac{1}{3}(\tilde{\alpha}_{xx} + \tilde{\alpha}_{yy} + \tilde{\alpha}_{zz}), \tag{2}$$

$$\beta^2 \equiv \frac{1}{2}\{(\tilde{\alpha}_{xx} - \tilde{\alpha}_{yy})^2 + (\tilde{\alpha}_{yy} - \tilde{\alpha}_{zz})^2 + (\tilde{\alpha}_{zz} - \tilde{\alpha}_{xx})^2$$
$$+ 6[(\tilde{\alpha}_{xy})^2 + (\tilde{\alpha}_{yz})^2 + (\tilde{\alpha}_{xz})^2]\}, \tag{3}$$

where $\tilde{\alpha}_s$ and β represent the isotropic and anisotropic parts of the derivative of the polarizability tensor with respect to the phonon normal mode, respectively. The importance of such representation is its invariance under a change in the sample orientation. Finally, using these forms of symmetric and antisymmetric polarizability derivative tensors, the Raman activity R_A can be written as

$$R_A = 45\tilde{\alpha}_s^2 + 7\beta^2. \tag{4}$$

In the rest of the paper, the Raman activities of PbI_2 crystals are calculated using Eq. (4).

III. MONOLAYER-TO-BULK PbI_2

A. Electronic-band structure

Like many TMDs, monolayer PbI_2 crystallizes in either the 1H or 1T phase. It was already demonstrated that the 1T phase is the structural ground state of monolayer PbI_2 [50]. In the present study, we consider the 1T phase for PbI_2 crystal (see Fig. 1). 1T phase of bulk and monolayer PbI_2 can be represented by a three-atom primitive unit cell. The bulk crystal is composed of weakly vdW interacting PbI_2 layers. In an isolated monolayer crystal, a layer of Pb atoms is sandwiched between two layers of I atoms which corresponds to the space group $P\bar{3}m2$. Each Pb atom is surrounded by six I atoms forming a near-octahedral $[PbI_6]^{4-}$ unit. When sharing edges with six neighboring octahedra a monolayer of PbI_2 is constituted (see left panel of Fig. 1). The calculated in-plane

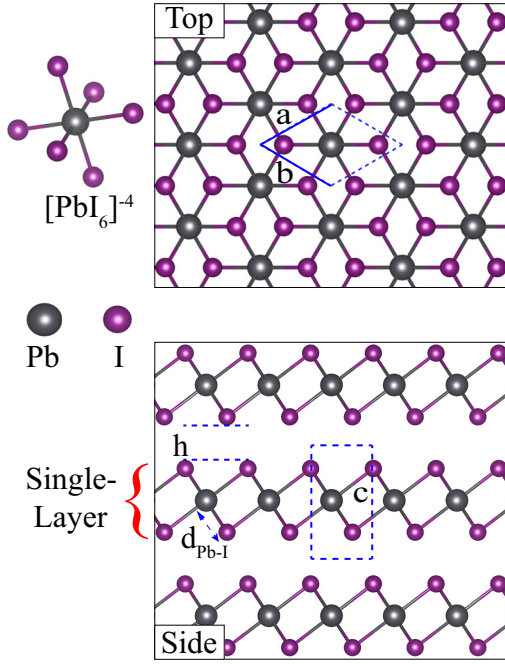FIG. 1. Top and side views of bulk PbI$_2$. The lattice parameters a, b, and c, the octahedral unit [PbI$_6$]$^{-4}$, layer thickness, and Pb-I atomic bond length $d_{\text{Pb-I}}$, are shown in the inset of the figures. For the visualization of the atomic structure the software VESTA was used [49].

and out-of-plane lattice parameters for the bulk crystal are 4.45 and 7.09 Å, respectively. The Pb-I atomic bond length is 3.23 Å while the interlayer distance is 3.18 Å. In the case of few-layer PbI$_2$ crystals, the in-plane lattice constant slightly decreases (4.44 Å) with the corresponding Pb-I bond length of 3.24 Å. Thus, it is important to note that the structural parameters are almost independent on the number of layers of PbI$_2$. Bader charge analysis shows that an amount of $\sim 0.4\, e^-$ is received by an I atom indicating the ionic bonding character between Pb and I atoms. In addition, as listed in Table I, the work function (Φ), which is defined for a semiconductor as the amount of energy required to remove a charge carrier located at the Fermi energy to vacuum as a free particle, decreases rapidly from monolayer to 4L crystal and then slowly upon

TABLE I. From bulk to monolayer PbI$_2$ crystal, the thickness of PbI$_2$ layers h and energy band gaps including SOC ($E_{\text{gap}}^{\text{SOC}}$) and HSE06 ($E_{\text{gap}}^{\text{HSE06+SOC}}$). Location of VBM and CBM edges in the BZ, and the work function Φ.

	h (Å)	$E_{\text{gap}}^{\text{SOC}}$ (eV)	$E_{\text{gap}}^{\text{SOC+HSE06}}$ (eV)	VBM/CBM	Φ (eV)
1L-PbI$_2$	7.13	1.99	2.65	M-Γ/Γ	6.10
2L-PbI$_2$	21.39	1.75	2.39	M-Γ/Γ	5.99
3L-PbI$_2$	28.52	1.62	2.23	Γ/Γ	5.93
4L-PbI$_2$	35.65	1.50	2.18	Γ/Γ	5.84
5L-PbI$_2$	42.78	1.47	2.14	Γ/Γ	5.82
6L-PbI$_2$	49.91	1.45	2.11(2.38) [18]	Γ/Γ	5.80
Bulk-PbI$_2$	–	1.40	2.07(2.41) [18]	A/A	–

further increasing the number of layers. The reason for such decrease is that as the number of layers increases, the number of electrons also increases which sets the Fermi level to higher energies. This leads to a decrease in work function which is the energy difference between the vacuum level and the Fermi level.

In order to understand the effect of the thickness on the electronic properties of PbI$_2$ crystals, we perform electronic-band structure calculations for different thicknesses of PbI$_2$ crystals (1L, 2L, 3L, 4L, 5L, 6L, and bulk). As shown in Fig. 2(a), the conduction band minimum (CBM) is located at the Γ point in the BZ for all PbI$_2$ crystals. However, as the number of layers increases from 1L to 3L, the valence band maximum (VBM) shifts from between the Γ and K points to the Γ point which indicates a transition from indirect-to-direct band gap for 3L-PbI$_2$. In this section we give our HSE06+SOC band gap results which approximately gives the correct band gap for PbI$_2$. The indirect band gap values are 2.65 and 2.39 eV for 1L and 2L crystals, respectively. For 3L and thicker structures, the VBM shifts to the Γ point and the direct band gap for 3L-PbI$_2$ is 2.23 eV. The thickness of 3L-PbI$_2$ (~ 2.9 nm) seems to be the critical thickness for such an indirect-to-direct band gap transition. As the number of layer increases to 6L, the band gap decreases to 2.11 eV and saturates to 2.07 eV for bulk-PbI$_2$ (see Fig. 2). Our results for the direct-to-indirect band gap transition agree with those reported by Toulouse *et al.* [21]. However, quantitative differences between our band gap results and theirs are due to the use of different functionals. Different from the methodology used by Toulouse *et al.* [21], we consider the GGA functional within vdW correction which is very important for layered materials. Although, it was pointed out by Toulouse *et al.*, the nature of the band gap transition in PbI$_2$ is explained through layer-layer interaction while the change in the band gap is driven by both quantum confinement and vdW interlayer interaction. In addition, we aim to understand the behavior of the band gap with the number of layers by fitting the band gap values to a functional of the form given in Eq. (5).

In order to compare with the usual particle in a box model for quantum confinement for which the energy decays as $\sim 1/N^2$ [51], we fitted the band gap to a general power law of the form [52]

$$E_{\text{gap}}(N) = E_{\text{gap}}(\text{bulk}) + \frac{A}{N^\kappa}, \qquad (5)$$

where N is the number of layers. The value $E_{\text{gap}}(\text{bulk})$, 2.07 eV, is the bulk band gap and we obtain κ and A to be 1.3 and 0.6 eV, respectively. Here since two different physical mechanisms drive the changes in the band structures, one may also try to fit the band gap change to a function including both exponential and power-law forms as suggested by Rudenko *et al.* [53]. In addition, Tran *et al.* [52] demonstrated that the quantum confinement exponent may give different values for the band gap fits calculated at different levels of the theory (PBE, GW,...). Indeed, it should be noted that the change in the band gap is different from 1L-to-3L and from 4L-to-bulk. In the first thickness regime, the orbital-orbital interaction between neighboring PbI$_2$ layers dominate the vdW interaction
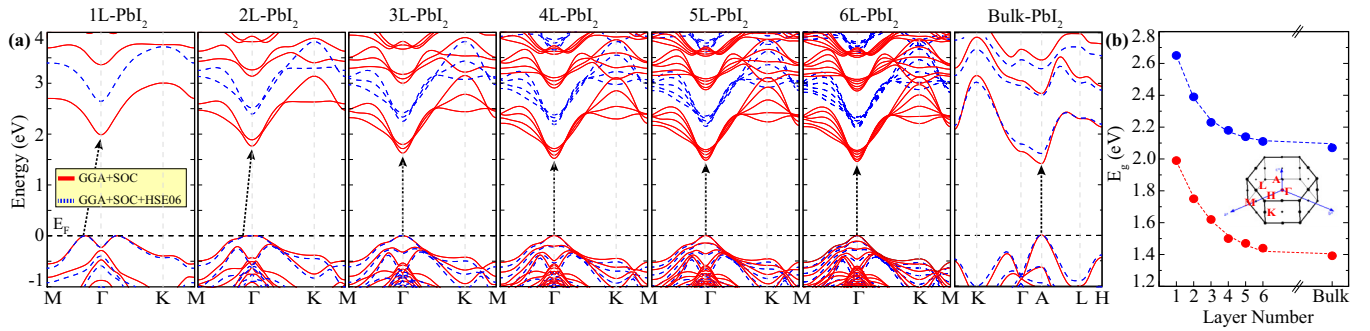
FIG. 2. (a) Evolution of electronic-band structure from monolayer to bulk crystal of PbI_2. The Fermi energy (E_F) level is set to the valence band maximum. The red solid and blue dashed lines represent the band structures calculated within SOC and HSE06 on top of GGA, respectively. (b) The change of band gap with respect to the number of layers. The inset shows the high symmetry points in the BZ.

and drives the indirect-direct band gap transition. However, for thicker crystals the electrons are mostly confined to the layers and the relatively small decrease in the band gap can be attributed to weak interactions between the layers (vdW, Coulomb, etc.)

The transition from indirect-to-direct band gap semiconducting behavior can be attributed to the orbital hybridizations between I atoms from the nearest-neighboring layers. As shown in Fig. 3, in monolayer PbI_2 the VBM is composed of mixed in-plane p orbitals (p_x and p_y). When the second layer is introduced, i.e., the bilayer case, the VBM is composed of tilted-interacting p_z orbitals of the I atoms. As the number of layers increases to 3, the hybridization between the I atoms from neighboring layers converts the VBM orbitals completely to p_z orbitals which controls the indirect-to-direct band gap semiconducting transition. In few-layer PbI_2 crystals, it is seen that this hybridization mostly occurs between the I atoms of the internal layers and thus the contributions from the outer layers become negligible. In contrast to the VBM, the CBM consists of p orbitals of the Pb atoms which are located at the center of each layer. The CBM has no thickness dependency since there is no direct interaction between the Pb atoms of the neighboring layers.
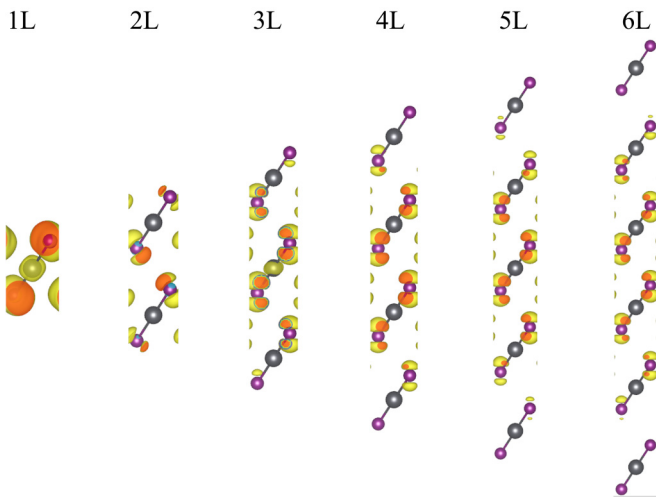

FIG. 3. Atomic orbital character of the valence band maximum of PbI_2 crystals from 1L to 6L. The isosurface value is 5×10^{-6} $e/Å^3$. The atomic orbitals were visualized using the software VESTA [49].

B. Phonons and Raman spectrum

In this section we discuss the thickness dependency of the phononic properties of PbI_2, through high-frequency optical phonons and low-frequency layer breathing (LB), and interlayer shear (C) modes by considering their frequencies and Raman activities. Note that, in crystals where vacuum is introduced, the Raman activities are normalized with respect to vacuum by using the thickness h (see Table I) of the PbI_2 crystals.

The dynamical stability of each PbI_2 crystal is examined by calculating the corresponding phonon band structure through the whole BZ. As shown in Fig. 4, all crystals are dynamically stable with no significant imaginary frequencies. Small negative frequencies in the out-of-plane acoustic (ZA) mode near the Γ point are attributed to numerical artifacts which are caused by small inaccuracies of the FFT grid. To determine the first-order off-resonant Raman spectrum, we calculate the zone-centered vibrational phonon modes at the Γ point of the BZ. For a PbI_2 crystal there are two types of Raman modes, E_g and A_{1g}. The E_g modes are doubly degenerate and arise from the opposite in-plane vibration of two I atoms with respect to the Pb atom, while the A_{1g} mode is associated with the out-of-plane vibration of only I atoms in the opposite direction (Fig. 5). Apart from those optical Raman modes, there are also low-frequency phonon modes which appear in the Raman spectrum in the low frequency region (generally below 50 cm^{-1}). These low-frequency modes are categorized into two types: in-plane C and out-of-plane LB vibrational modes.

Initially, the majority of research activities in layered materials focused on analyzing high-frequency optical phonon modes which involve vibrations of atoms that stem from the intralayer chemical bonds. These phonon modes, which are called intralayer modes, the restoring forces are dominated by the strength of the intralayer chemical bonds rather than the vdW type forces which hold the layers together. Because of this reason, high-frequency intralayer modes are not very sensitive to the interlayer coupling, and therefore they are of limited use in the determination of thickness and stacking order.

1. High-frequency optical modes

As given in Table II, the peak frequencies of E_g and A_{1g} harden as the number of layers increases which is attributed to the interlayer vdW forces suppressing atomic vibrations.
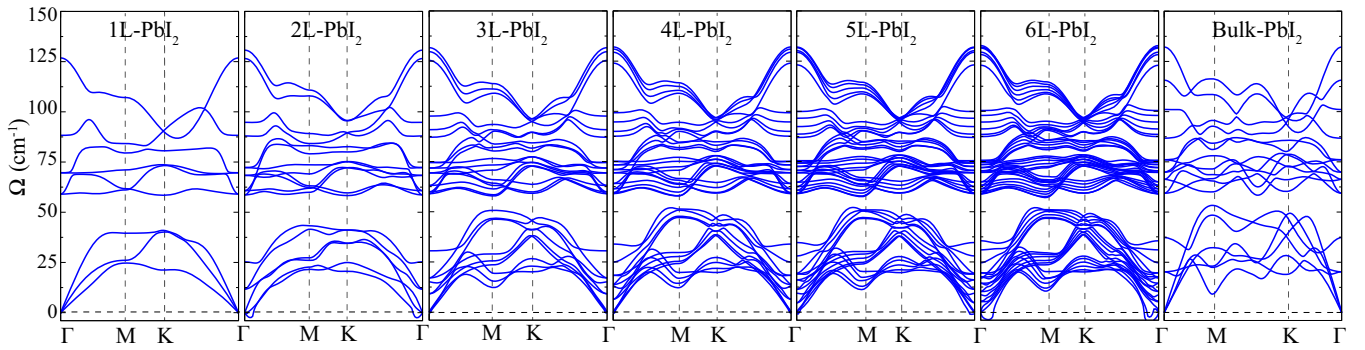
FIG. 4. The phonon-band structures of PbI$_2$ crystals from monolayer to bulk.

The frequency of A_{1g} mode displays a hardening from 87.6 to 101.1 cm^{-1} when going from monolayer to bulk. In the case of E_g mode, the corresponding frequency shifts from 68.5 to 75.8 cm^{-1}. The relative shift of both phonon modes $\Delta\Omega_{A_{1g}}$ and $\Delta\Omega_{E_g}$ are calculated by using

$$\Delta\Omega_i = \frac{\Omega_i(N) - \Omega_i(N-1)}{\Omega_i(N)}, \qquad (6)$$

and listed in Table II. As seen in Fig. 6(a), as the number of layers increases the shift rate decreases and saturates to the bulk limit.

As in the case of the energy band gap, the evolution of the phonon frequencies with the number of layers can be fitted by the formula [54,55]

$$\Omega(N) = \Omega_{\text{bulk}} - D \frac{a}{N^\gamma}, \qquad (7)$$

where Ω_{bulk} is the frequency of the optical phonon mode for bulk crystal and $a = 4.45 \times 10^{-8}$ cm is the lattice constant of bulk. D and γ are fitting parameters that match the N-dependent Raman shifts. For both of the prominent optical phonons A_{1g} and E_g, the calculated frequencies are fitted to Eq. (7) and the fitted frequencies are listed in Table II and also are shown in Fig. 6(a). When the calculated frequencies are fitted for A_{1g}, the parameters D and γ are found to be 1.55×10^{-8} 1/cm^2 and 1.83, respectively which gives the best fit to our calculated frequencies. In the case of E_g

phonon mode, $\gamma = 1.83$ is found to be the same while $D = 0.64 \times 10^{-8}$ 1/cm^2 is smaller than that for A_{1g}. When fitting the calculated frequencies, the frequencies of the 1L crystal are omitted because they do not exhibit the same trend of the few-layer structures. This is mainly attributed to the layer-layer interaction. As given in Table II, the frequency shift rates of both phonon modes are largest when going from the 1L crystal to the 2L crystal. This is can be understood as follows: addition of a second layer induces additional springs between the layers that significantly increases the frequency. Our fitted function can be used to calculate the frequencies of both phonon modes for arbitrary thickness of PbI$_2$. Zhong *et al.* [18] reported the frequency of A_{1g} mode for 2L-, 9L-, and bulk-PbI$_2$ to be approximately equal ($\sim$ 96 cm^{-1}) while we find (see Table II) that they can differ by almost 5 cm^{-1}.

The suppression of atomic vibrations by the layer-layer vdW interaction is more dominant in bilayer and trilayer cases as supported by the values listed in Table II. As the number of layers increases, the relative contribution of the interaction with the outer neighboring layers decreases and thus, the change in the frequency gets smaller. The main contribution from the vdW interaction stems from the nearest-neighboring layers in the center of the few-layer sample.

Zhang *et al.* [33] developed a diatomic chain model (DCM) for the intralayer shear (E_g) and breathing (A_{1g}) modes that can explain the nature of the force constants per unit area, $\alpha_{\text{Pb-I}}^{\parallel}$ and $\alpha_{\text{Pb-I}}^{\perp}$, which are needed to describe the interaction between Pb and I atoms in a monolayer. Here the component $\alpha_{\text{Pb-I}}^{\parallel}$ describes
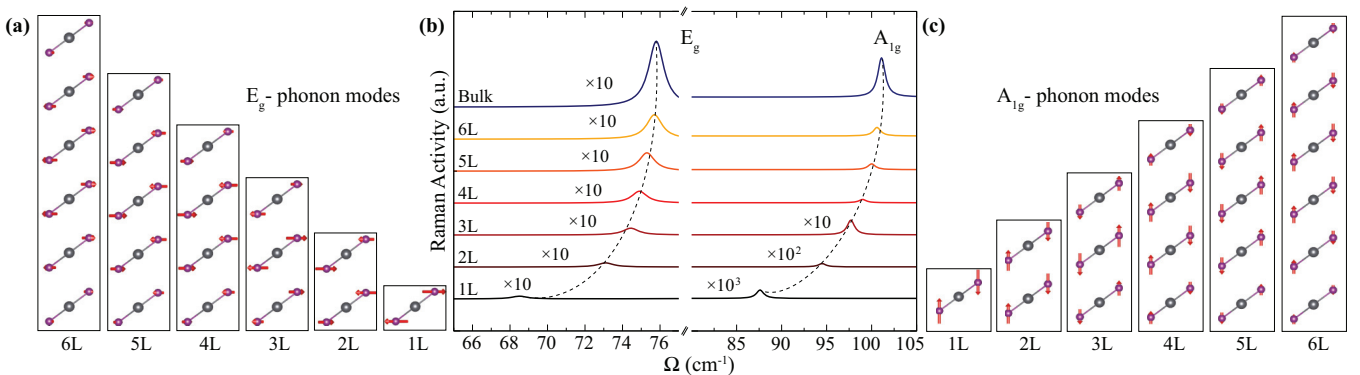

FIG. 5. (a) The vibrational motion of I atoms in E_g phonon modes for a different number of PbI$_2$ layers. (b) The evolution of Raman spectrum with respect to the number of layers for the two characteristic prominent peaks. (c) The vibrational motion of I atoms in A_{1g} phonon mode.

TABLE II. From bulk to monolayer PbI_2: calculated and fitted peak positions of the Raman active phonon modes, E_g(calc), E_g(fit), A_{1g}(calc), and A_{1g}(fit), the relative frequency shift of each phonon mode with respect to the frequency of the mode in $(N-1)$-PbI_2, $\Delta\Omega_{A_{1g}}$, and $\Delta\Omega_{E_g}$. The Raman activity of phonon modes and their relative ratios, I_{E_g}, $I_{A_{1g}}$, and $\frac{I_{A_{1g}}}{I_{E_g}}$. The in-plane ($\epsilon_{in}$) and out-of-plane ($\epsilon_{out}$) static (low-frequency) dielectric constant. The frequencies given in the parentheses are from the literature.

| | E_g(calc) | E_g(fit) | A_{1g}(calc) | A_{1g}(fit) | $\Delta\Omega_{A_{1g}}$ | $\Delta\Omega_{E_g}$ | I_{E_g} | $I_{A_{1g}}$ | $\frac{I_{A_{1g}}}{I_{E_g}}$ | ϵ_{in} | ϵ_{out} |
	(cm^{-1})	(cm^{-1})	(cm^{-1})	(cm^{-1})	(%)	(%)	($\frac{Å^4}{amu}$)	($\frac{Å^4}{amu}$)			
1L-PbI$_2$	68.5	–	87.6	–	–	–	1.3	0.1	0.1	2.56	1.30
2L-PbI$_2$	73.1	73.0	94.5(96.0) [18]	94.4	7.9	6.7	2.0	3.2	1.6	3.24	1.49
3L-PbI$_2$	74.4	74.5	97.7	97.9	3.4	1.9	3.3	14.3	4.3	3.84	1.70
4L-PbI$_2$	74.9	75.0	99.0	99.2	1.3	0.6	5.8	32.0	5.5	4.28	1.89
5L-PbI$_2$	75.3	75.3	100.0	99.9	1.0	0.5	9.0	56.5	6.3	4.68	2.06
6L-PbI$_2$	75.7	75.5	100.6	100.2	0.6	0.5	12.0	83.7	7.0	4.81	2.18
Bulk-PbI$_2$	75.8	75.8	101.1(96.0) [18]	101.1	–	–	32.3	384.4	11.9	6.87	5.68

the in-plane lattice dynamics while the $\alpha_{Pb-I}^{\perp}$ determines that of the out-of-plane dynamics between Pb and I atoms. For these two optical phonon modes, the force constant per unit area can be related to the phonon frequency by the equations [33]

$$\Omega_{A_{1g}} = \left(\frac{1}{\sqrt{2}\pi c}\right)\sqrt{\frac{2\alpha_{Pb-I}^{\perp}}{\mu}},$$

$$\Omega_{E_g} = \left(\frac{1}{\sqrt{2}\pi c}\right)\sqrt{\frac{2\alpha_{Pb-I}^{\parallel}}{\mu}}, \qquad (8)$$

where μ is the atomic mass per unit area and c is the speed of light. Due to the vibration of I atoms, the total mass per unit area is equal to $2m_I$. Using the frequencies of A_{1g} (87.6 cm^{-1}) and E_g (68.5 cm^{-1}) in 1L-PbI$_2$ and the mass density of I atom ($m_I = 1.24 \times 10^{-4}$ kg/m^2), we find the $\perp$ and $\parallel$ components of the force constant per unit area as $\alpha_{Pb-I}^{\perp} = 0.34 \times 10^{21}$ N/m^3 and $\alpha_{Pb-I}^{\parallel} = 0.21 \times 10^{21}$ N/m^3 which are approximately 10 times smaller than those for MoS$_2$ (3.46×10^{21} and 1.88×10^{21} N/m^3, respectively) [33]. As listed in Table IV, the $\alpha_{Pb-I}^{\parallel}$ is also much smaller than that of graphene (33.8×10^{21} N/m^3) [34] indicating the strong C-C bonds in graphene that results in a high frequency for the in-plane mode in graphene.

It has been shown for many other 2D layered materials that not only the peak frequencies but also the activities of Raman active modes are also key for the determination of the number of layers [56–58]. In the present study we calculate the first order off-resonant Raman activities of two prominent, high-frequency optical phonons E_g and A_{1g} for monolayer, few-layer, and bulk PbI$_2$ crystals. First of all, the individual Raman activities of each phonon mode display an increasing trend with an increasing number of layers. Only in the monolayer limit, the Raman activity of A_{1g} mode is much lower than that of E_g. In bilayer and few-layer cases, the contribution of both in-plane and out-of-plane dielectric constants to the Raman tensor increases. The reason why the increment in activity of A_{1g} is much larger than that of E_g can be explained through the Raman tensors of the two peaks. The Raman tensors of the two peaks are known from group symmetry of the crystal

structure as

$$R_{A_{1g}} = \begin{bmatrix} a & 0 & 0 \\ 0 & a & 0 \\ 0 & 0 & b \end{bmatrix},$$

$$R_{E_g} = \begin{bmatrix} c & 0 & 0 \\ 0 & -c & d \\ 0 & d & 0 \end{bmatrix}, \begin{bmatrix} 0 & -c & d \\ -c & 0 & 0 \\ d & 0 & 0 \end{bmatrix},$$

where a, b, c, and d are the derivative of the polarizability with respect to the considered normal mode. Since E_g is doubly degenerate, the total Raman activity is the sum of the activities of two tensors standing for longitudinal and transverse orientations. In contrast to the Raman tensors of E_g mode, there is an out-of-plane contribution of the derivative of polarizability in the Raman tensor of A_{1g} (the number b). It can be clearly seen that increasing the in-plane dielectric constant from monolayer to bulk affects the Raman tensors of both modes (i.e., the values of R_{11} and R_{22} are affected). However, increasing the number of layers results in an increase of out-of-plane dielectric constant which only influences the Raman activity of the A_{1g} mode. Another reason for the higher increase of Raman activity of A_{1g} is the contribution of the isotropic part of polarizability derivatives to the Raman activity. As given in Eq. (4), the isotropic part $\tilde{\alpha}_s^2$ is the sum
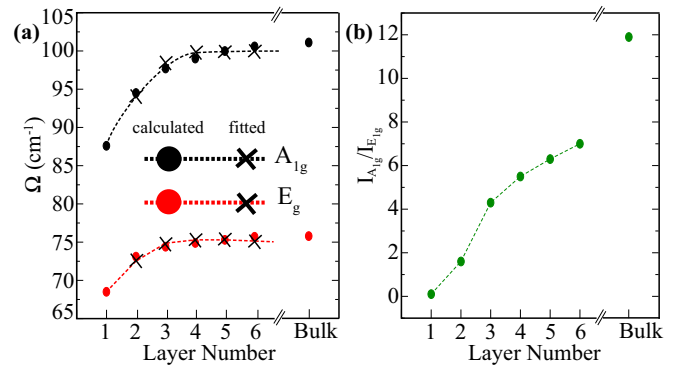

FIG. 6. (a) The shifts in frequencies of E_g and A_{1g} vibrational modes with respect to the number of layers. (b) The change in Raman activity ratio of the two prominent peaks as a function of the number of the layers.

of the squares of the diagonal terms which is dominant in the anisotropic part β^2.

Also it should be noted that in Raman experiments a certain polarization direction is used to detect the Raman active phonon modes. As seen from the Raman tensors, the A_{1g} mode is observable for only certain polarization angles while the E_g mode is always observable independent of the polarization angle of the incident light. For a backscattering configuration, the polarization vector of incident (e_i) and scattered (e_s) light are in the xy plane. These two vectors can be represented in terms of an angle θ which is the angle between the polarization vectors of incident and scattered light. Setting e_i as ($\cos\theta, \sin\theta, 0$) and e_s as (1, 0, 0), one may calculate the Raman activities to be proportional to $a^2 \cos^2\theta$ for A_{1g} and proportional to c^2 for E_g mode. Thus, the activity of E_g mode is independent of the polarization angle θ while that of A_{1g} is only nonzero when the polarization directions of incident and scattered lights are not perpendicular to each other.

Since measured Raman intensities are taken on different substrates, the Raman intensities can also vary for different experimental setups (i.e., for different laser energies). Therefore, the discussion of relative Raman activities of the two prominent peaks seems to be more reliable for the determination of the number of layers in layered materials. In this section we discuss the Raman activity ratio of A_{1g} to that of E_g, i.e., $\frac{I_{A_{1g}}}{I_{E_g}}$. Our results reveal that in the monolayer limit, the Raman activity of A_{1g} mode is lower than that of E_g and the corresponding ratio is about 0.1 [see Fig. 6(b)]. Thus, the relative activity of A_{1g} can be used to determine the thickness of a PbI$_2$ sample, i.e., the number of layers. As the numbers of layer increases, the Raman activity of A_{1g} becomes dominant to that of E_g and the ratio increases even in the bilayer case.

2. Interlayer shear and layer breathing modes

Zero shift corresponds to Rayleigh (elastic) scattering of photons which has a very high intensity as compared to inelastically scattered photons. Since the interlayer C and LB phonons have usually very low frequencies (several to tens of wave numbers), the probing of these phonons through Raman spectroscopy is challenging. The low-frequency characteristic of the interlayer C and LB phonon modes actually results from the weak interlayer vdW restoring force. It was shown for other layered materials, such as graphene and MoS$_2$, that these low-frequency phonon modes give information about the number of layers N since the vibrations themselves are rigid motions of each layer. In contrast to the high-frequency optical phonons, the interlayer modes have low frequencies and are almost completely determined by the interlayer restoring forces. The weak nature of the vdW layer-layer interaction and the fact that a large ensemble of atoms move together is responsible for the low frequencies which typically yields frequencies well below ~ 100 cm^{-1}. Due to their layer sensitivity to interlayer coupling, low-frequency Raman modes have recently started to attract increasing attention for the determination of the interfacial coupling and the thickness of the sample [34].

Interlayer shear (C) modes:. The interlayer C modes are assigned to the in-plane rigid-layer vibrations of each PbI$_2$ layer. The frequencies of C and LB modes are smaller than ~ 50 cm^{-1} which is a natural result of the weak vdW forces.
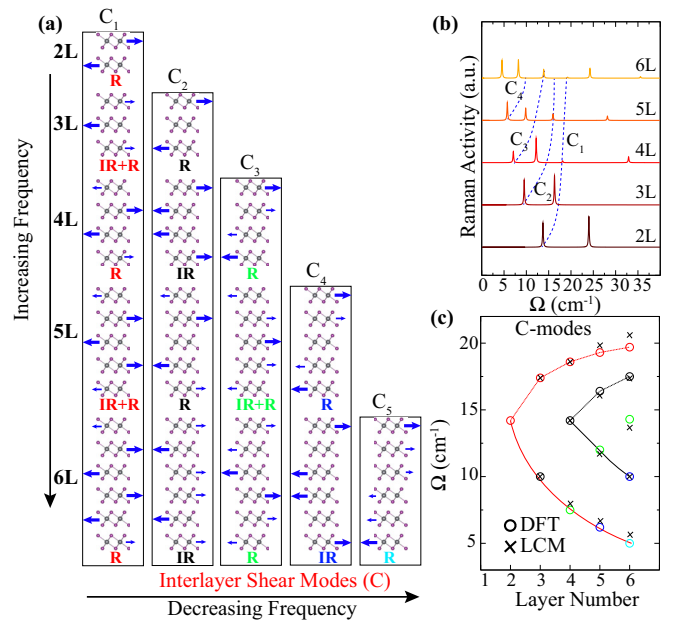

FIG. 7. (a) The vibrational character of interlayer C modes from 2L-to-6L. The Raman activity (R) and infrared activity (IR) of each phonon mode are given below the mode. The same colors correspond to the same phonon modes in different few-layer PbI$_2$. (b) The Raman spectrum of low-frequency interlayer C phonon modes for a different number of layers of PbI$_2$ crystal. (c) The change in frequency of interlayer C modes. Results of DFT calculations and LCM are compared.

1T-PbI$_2$ belongs to the D_{3d} point group which is independent of the number of layers. In contrast, the Raman or infrared activity of a C mode strongly depends on whether N is even or odd.

For the N-layer PbI$_2$ sample, one should count $2 \times (N-1)$ C modes where the coefficient 2 corresponds to the degeneracy of the modes. The C modes are either Raman or infrared active for even number PbI$_2$ (EN-PbI$_2$) layers while for odd number PbI$_2$ layers (ON-PbI$_2$), they are either Raman active or both infrared and Raman active. As seen in the right panel of Fig. 6, one C mode appears in 2L-PbI$_2$. As the number of layers becomes three, this mode splits into two branches one of which hardens and the other softens with increasing N. So for each number of layers, an additional mode appears with increasing N. As seen in Fig. 6(b) connecting each branch of the C modes with dashed and solid lines shows a series of conelike curves. For example, the shear mode C$_1$ (denoted by red color) exhibits the opposite rigid vibration of each PbI$_2$ layer with respect to each other as shown in Fig. 6. As N increases from 2L-to-6L, its frequency hardens from 11.7 cm^{-1} in 2L-PbI$_2$ to 19.3 cm^{-1} in 6L-PbI$_2$ and reaches 20.3 cm^{-1} in bulk-PbI$_2$ (Fig. 7).

As modeled for other 2D layered materials, the physics of C and LB modes can be obtained using a simple linear chain model (LCM). Since each PbI$_2$ layer exhibits a rigid vibration, they can be considered as a single mass and then the LCM is constructed. Such approximation has been proven to work very well for 2D layered materials [33,34,59]. The frequency of C$_1$ in bulk crystal is related to that of 2L-PbI$_2$ by the relation

$$\Omega(C_{2,1}) = \Omega(C_{\text{bulk}})/\sqrt{2}. \qquad (9)$$

TABLE III. From 2L-to-6L PbI_2 crystal, the frequencies and Raman or infrared activity of C and LB modes. The following notations are used: R Raman active, IR Infrared active, and IR+R both infrared and Raman active.

	C_1 (cm^{-1})	C_2 (cm^{-1})	C_3 (cm^{-1})	C_4 (cm^{-1})	C_5 (cm^{-1})	LB_1 (cm^{-1})	LB_2 (cm^{-1})	LB_3 (cm^{-1})	LB_4 (cm^{-1})	LB_5 (cm^{-1})
2L-PbI_2	14.2 (R)	–	–	–	–	24.5 (R)	–	–	–	–
3L-PbI_2	17.4 (IR+R)	10.0 (R)	–	–	–	16.8 (R)	30.8 (IR)	–	–	–
4L-PbI_2	18.6 (R)	14.2 (IR)	7.5 (R)	–	–	12.7 (R)	24.4 (IR)	33.4 (R)	–	–
5L-PbI_2	19.3 (IR+R)	16.4 (R)	12.0 (IR+R)	6.2 (R)	–	10.3 (R)	20.1 (IR)	28.6 (R)	34.9 (IR)	–
6L-PbI_2	19.7 (R)	17.5 (IR)	14.3 (R)	10.0 (IR)	5.0 (R)	8.7 (R)	17.0 (IR)	24.7 (R)	31.1 (IR)	36.1 (R)

Using the relation given by Eq. (9), the frequency of C_1 in the bulk limit is calculated to be 20.1 cm^{-1} which is very close to that of bulk crystal (20.3 cm^{-1}) calculated within DFT. By the same methodology, one can calculate the frequencies of all C modes for bulk crystals by using the calculated C_i values which are listed in Table III.

As we relate the bulk frequency of a C mode to its frequency in N-PbI_2 by Eq. (9), it is also possible to generate all the C mode frequencies from that of the 2L-PbI_2 crystal. As stated by Zhang *et al.* [33], their LCM is applicable to any layered material. They reported that the general approach is to calculate the μ for the monolayer of a given material, and then from the knowledge of the frequency of C in 2L sample, one can predict the relation between the frequency and N for the different branches in any layered material. The relation between the frequency of C modes with N is given by the formula

$$\Omega_C(N) = \Omega_C(2)\sqrt{1 \pm \cos\left(\frac{N_0\pi}{N}\right)}, \qquad (10)$$

where $\Omega_C(N)$ is the frequency of the C mode in N-PbI_2 while $\Omega_C(2)$ represents that of the 2L sample and N_0 is an integer, $N_0 = 1, 2, 3, 4, \ldots$. As listed in Table III, the frequency of C in 2L-PbI_2 is found to be 14.3 cm^{-1}. Using Eq. (10), one can find the frequencies of the two branches in 3L-PbI_2 which are 17.5 and 10.1 cm^{-1} for the higher and lower branches, respectively. These values are very close to the frequencies calculated directly by the small displacement method (17.4 and 10.0 cm^{-1} for higher and lower branches, respectively). It is obvious that for the C modes in layered materials, the LCM matches well with the calculated frequencies using the small-displacement methodology.

As in the case of high-frequency optical modes, the interlayer C mode frequency can also be represented in terms of the force constant per unit area α and the reduced mass of a rigid layer μ as

$$\Omega_C = \left(\frac{1}{\sqrt{2}\pi c}\right)\sqrt{\frac{\alpha^{\parallel}_{I-I}}{\mu}}, \qquad (11)$$

where $\alpha^{\parallel}_{I-I}$ denotes the in-plane nearest-neighboring interlayer force constant per unit area between two I atoms and c is the speed of light. Because of the rigid vibration of each layer,

one can assume one layer as a ball with mass $m_{Pb} + 2m_I$. This relation allows us to calculate the force constant $k^{\parallel}_{I-I} = A\alpha^{\parallel}_{I-I}$ where A is the area of the unit cell. The individual mass densities of Pb and I atoms per unit cell area are $m_{Pb} = 2.02 \times 10^{-7}$ and $m_I = 1.24 \times 10^{-4}$ kg/m^2, respectively. Now, using these mass densities in Eq. (11) we find the interlayer force constant per unit area $\alpha^{\parallel}_{I-I}$ for the C mode in 2L-PbI_2 as $\alpha^{\parallel}_{I-I} = 1.61 \times 10^{19}$ N/m^3 which is lower than that reported for MoS_2 (2.82×10^{19} N/m^3) [33] (see Table IV). This is exactly the reason why the frequency of C mode in 2L-PbI_2 (14.3 cm^{-1}) is lower than that of 2L-MoS_2 (23.0 cm^{-1}) [33]. It is also possible to calculate the force constant $k^{\parallel}_{I-I}$ between two PbI_2 layer by multiplying $\alpha^{\parallel}_{I-I}$ by the unit cell area which gives 2.8 N/m which is slightly larger than that reported for MoS_2 (2.7 N/m) [33]. Moreover, the interlayer shear modulus can also be calculated by multiplying $\alpha^{\parallel}_{I-I}$ by the equilibrium distance between two adjacent PbI_2 layers which is the effective thickness of the monolayer crystal (7.13 Å). The corresponding shear modulus is found to be 11.6 GPa which is lower than that of MoS_2 (18.9 GPa) [33].

In addition to the peak frequencies, the Raman activity of the C modes strongly depends on the number of layers whether it is odd or even. The Raman activity of C_1 is distinguishable for EN-PbI_2 and ON-PbI_2 crystals. Our results reveal that the Raman activity values of C_1 in EN-PbI_2 are approximately 10^4 times that of ON-PbI_2. As listed in Table III, the C_2 modes are Raman active for ON-PbI_2 and infrared active for EN-PbI_2 and

TABLE IV. Parallel $\alpha^{\parallel}_{Pb-I}$ and perpendicular $\alpha^{\perp}_{Pb-I}$ force constants per unit area between Pb and I atoms. Those between I atoms from nearest-neighboring PbI_2 layers $\alpha^{\parallel}_{I-I}$, and $\alpha^{\perp}_{I-I}$. For comparison, the values for graphene and MoS_2 are also listed. The unit of the force constant per unit area is N/m^3.

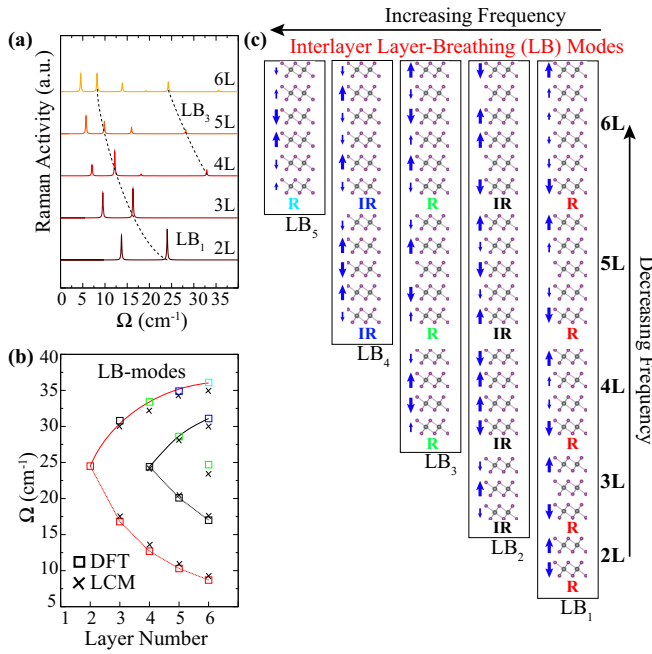|	$\alpha^{\parallel}_{Pb-I}$	$\alpha^{\perp}_{Pb-I}$	$\alpha^{\parallel}_{I-I}$	$\alpha^{\perp}_{I-I}$
PbI_2	0.21×10^{21}	0.34×10^{21}	1.61×10^{19}	4.78×10^{19}
	$\alpha^{\parallel}_{C-C}$	$\alpha^{\perp}_{C-C}$	$\alpha^{\parallel}_{C-C}$	$\alpha^{\perp}_{C-C}$
Graphene [34]	33.8×10^{21}	–	1.28×10^{19}	10.7×10^{19}
	$\alpha^{\parallel}_{Mo-S}$	$\alpha^{\perp}_{Mo-S}$	$\alpha^{\parallel}_{S-S}$	$\alpha^{\perp}_{S-S}$
MoS_2 [33]	1.88×10^{21}	3.46×10^{21}	2.82×10^{19}	8.90×10^{19}

FIG. 8. Left panel: (a) The Raman spectrum of low-frequency interlayer breathing mode (LB) and the phonon modes for a different number of layers of PbI_2 crystal. (b) The change in frequency of interlayer LB modes with respect to a number of layers. Results of DFT calculations and LCM are compared. (c) The vibrational character of interlayer LB modes from 2L-to-6L. The Raman activity (R) and infrared activity (IR) of each phonon mode are given below the mode.

its frequency hardens from 9.2 to 17.2 cm^{-1} from 3L-to-6L. The frequency evolution of the other C modes are also listed in Table III. As shown in the right panel of Fig. 6, for EN-PbI_2 crystals there are $\frac{N}{2}$ Raman active C modes while the remaining ($\frac{N}{2} - 1$) are infrared active. However, in the case of ON-PbI_2 the number of Raman active modes are ($\frac{N-1}{2}$) and the remaining half of the C modes are both infrared and Raman active.

Interlayer breathing (LB) modes:. In contrast to the C modes, the interlayer LB modes are assigned to the out-of-plane rigid-layer vibrations of each PbI_2 layer. There are $N - 1$ nondegenerate LB modes in an N-PbI_2 crystal. Similar to the case of C modes, as N increases each LB mode generates two branches one at higher and one at lower frequencies. The frequencies of the additional branches also obey the relation given in Eq. (10). Moreover, the bulk frequency of any LB mode can also be predicted by using the relation given in Eq. (9).

As in the case of the C modes, the total number of interlayer LB modes depend on the number of layers in the crystal. In an N-layer PbI_2, there exists ($N - 1$) LB modes which are nondegenerate. The LB modes are either Raman active or infrared active depending on the number of layers in the PbI_2 crystal. As shown in the right panel of Fig. 8, the Raman active LB modes exist when the vibration is totally symmetric with respect to an axis perpendicular to the out-of-plane direction. For those LB modes, the out-of-plane vibration of layers has mirror symmetry along the out-of-plane direction. However,

the infrared active LB modes do not exhibit such mirror symmetry that is why the dipole moment changes instead of the polarizability. As the number of layers increases, each LB branch generates additional branches one of which is Raman active and the other is infrared active. Thus, for EN-PbI_2 there occurs $\frac{N}{2}$ Raman active LB modes while the remaining ($\frac{N}{2} - 1$) are infrared active. In the case of ON-PbI_2 the number of Raman active modes is equal to the number of infrared active modes. By the same analogy with C modes, LB modes form a series of conelike curves as shown in Fig. 8(c). For example, the LB_1 (denoted by red color) demonstrates the opposite rigid vibration of each PbI_2 layer with respect to each other in out-of-plane direction as shown in Fig. 8(c). As N increases from 2-to-6, its frequency softens from 24.5 cm^{-1} in 2L-PbI_2 to 8.7 cm^{-1} in 6L-PbI_2. Moreover, the evolution of frequencies of LB modes with the number of layers N can be explained by the relation given in Eq. (10). For example, the LB mode of 2L-PbI_2 generates two additional branches in 3L-PbI_2 one with higher and the other with lower frequency. Using the frequency of 2L crystal we find the frequencies of the two branches in 3L-PbI_2 to be 30.0 and 17.3 cm^{-1} for the higher and lower branches, respectively. These results agree with the frequencies calculated by using the small-displacement methodology.

By using the relation given in Eq. (11), one can calculate the out-of-plane nearest-neighboring interlayer force constant per unit area between two I atoms as $\alpha_{I-I}^{\perp} = 4.78 \times 10^{19}$ N/m^3 which is approximately half of that of MoS_2 (8.90×10^{19} N/m^3) [33]. The corresponding interlayer force constant is $k_{I-I}^{\perp} = 8.2$ N/m which is slightly larger than the value for MoS_2 (7.8 N/m) [33]. The difference between the force constant per unit area is therefore due to the larger unit cell area of PbI_2 when compared with that of MoS_2. The value for PbI_2 is also smaller than that of graphene as listed in Table IV. The difference between different layered materials is due to the different interlayer interactions between the individual layers. Thus, it is possible to conclude that the interlayer interaction between PbI_2 layers in few-layer crystal is slightly smaller than those between graphene and MoS_2 layers. One also should note that as listed in Table IV, the interlayer force constants per unit area are approximately 100 times smaller than those for the intralayer which means that in layered materials the intralayer atomic bondings are much stronger than the interlayer atomic interactions.

The LB mode in 2L-PbI_2 is found to be Raman active with a relatively high Raman activity as shown in Fig. 6(a). As mentioned above, the generated branches harden with N and are Raman active for EN-PbI_2 whose Raman activity display a decreasing trend. Thus, its observation becomes more difficult as N increases. However, the soften one approximately conserves its Raman activity for different N values. The reason for such different behavior in Raman activity can be understood through the strength of the vibrations of each layer. For the LB modes which soften with an increasing number of layers, the vibration strength of the inner layers are much weaker than those of the outer layers. Apparently the change of the polarizability and its volume is large. However, in EN-PbI_2 for the LB modes which harden as the number of layers increase, strong vibrations occur between the layers in the middle of the crystal and thus, the change of polarizability occurs in a relatively smaller volume which gives much smaller Raman

activity. Although the Raman activity changes from one LB mode to another and for a different number of layers, the shift of the peak frequencies is more distinguishable for the determination of the layer-layer interaction and the number N of layers rather than the Raman activities of the LB modes.

IV. CONCLUSIONS

In the present study the number of layer-dependent electronic and vibrational properties of PbI_2 crystals were investigated by focusing on the evolution of the band gap, peak frequencies, and corresponding activities of the Raman active phonon modes. Our results revealed that the direct or indirect gap semiconducting character of PbI_2 crystals are strongly influenced by the number of layers. In addition, an indirect-to-direct band gap transition is predicted for 3L-PbI_2. The layer-dependent Raman spectrum revealed that both prominent optical peaks A_{1g} and E_g display phonon hardening with an increasing number of layers which is attributed to the interlayer vdW forces which suppress the atomic vibrations resulting in phonon hardening in directly stacked layered materials. More-over, the relative Raman activities of A_{1g} and E_g peaks display an increasing trend from monolayer to bulk samples due to the strong enhancement of activity of A_{1g} with increasing thickness which is especially important for the determination of the monolayer PbI_2. We further characterized rigid-layer vibrations both for shear (C) and layer-breathing (LB) modes of few-layer PbI_2. Our study reveals that a reduced monoatomic (linear) chain model (LCM) provides a fairly accurate picture of the thickness dependence of the low-frequency modes and is also a powerful tool to study the interlayer coupling strength in layered PbI_2.

[1] K. S. Novoselov, A. K. Geim, S. V. Morozov, D. Jiang, Y. Zhang, S. V. Dubonos, I. V. Grigorieva, and A. A. Firsov, Science **306**, 666 (2004).

[2] K. S. Novoselov, A. K. Geim, S. V. Morozov, D. Jiang, M. I. Katsnelson, I. V. Grigorieva, S. V. Dubonos, and A. A. Firsov, Nature (London) **438**, 197 (2005).

[3] S. Cahangirov, M. Topsakal, E. Akturk, H. Sahin, and S. Ciraci, Phys. Rev. Lett. **102**, 236804 (2009).

[4] A. Kara, H. Enriquez, A. P. Seitsonen, L. C. L. Y. Voon, S. Vizzini, B. Aufray, and H. Oughaddou, Surf. Sci. Rep. **67**, 1 (2012).

[5] H. Sahin, S. Cahangirov, M. Topsakal, E. Bekaroglu, E. Akturk, R. T. Senger, and S. Ciraci, Phys. Rev. B **80**, 155453 (2009).

[6] Q. Wang, Q. Sun, P. Jena, and Y. Kawazoe, ACS Nano **3**, 621 (2009).

[7] K. K. Kim, A. Hsu, X. Jia, S. M. Kim, Y. Shi, M. Hofmann, D. Nezich, J. F. Rodriguez-Nieva, M. Dresselhaus, T. Palacios, and J. Kong, Nano Lett. **12**, 161 (2012).

[8] P. Tsipas, S. Kassavetis, D. Tsoutsou, E. Xenogiannopoulou, E. Golias, S. A. Giamini, C. Grazianetti, D. Chiappe, A. Molle, M. Fanciulli, and A. Dimoulas, Appl. Phys. Lett. **103**, 251605 (2013).

[9] C. Bacaksiz, H. Sahin, H. D. Ozaydin, S. Horzum, R. T. Senger, and F. M. Peeters, Phys. Rev. B **91**, 085430 (2015).

[10] R. A. Gordon, D. Yang, E. D. Crozier, D. T. Jiang, and R. F. Frindt, Phys. Rev. B **65**, 125407 (2002).

[11] J. N. Coleman, M. Lotya, A. O'Neill, S. D. Bergin, P. J. King, U. Khan, K. Young, A. Gaucher, S. De, R. J. Smith, I. V. Shvets, S. K. Arora, G. Stanton, H. Y. Kim, K. Lee, G. T. Kim, G. S. Duesberg, T. Hallam, J. J. Boland, J. J. Wang, J. F. Donegan, J. C. Grunlan, G. Moriarty, A. Shmeliov, R. J. Nicholls, J. M. Perkins, E. M. Grieveson, K. Theuwissen, D. W. McComb, P. D. Nellist, and V. Nicolosi, Science **331**, 568 (2011).

[12] Q. H. Wang, K. Kalantar-Zadeh, A. Kis, J. N. Coleman, and M. S. Strano, Nat. Nanotech. **7**, 699 (2012).

[13] J. S. Ross, P. Klement, A. M. Jones, N. J. Ghimire, J. Yan, D. G. Mandrus, T. Taniguchi, K. Watanabe, K. Kitamura, W. Yao, D. H. Cobden, and X. Xu, Nat. Nanotech. **9**, 268 (2014).

[14] H. Sahin, S. Tongay, S. Horzum, W. Fan, J. Zhou, J. Li, J. Wu, and F. M. Peeters, Phys. Rev. B **87**, 165409 (2013).

[15] S. Tongay, H. Sahin, C. Ko, A. Luce, W. Fan, K. Liu, J. Zhou, Y. S. Huang, C. H. Ho, J. Yan, D. F. Ogletree, S. Aloni, J. Ji, S. Li, J. Li, F. M. Peeters, and J. Wu, Nat. Commun. **5**, 3252 (2014).

[16] S. Horzum, D. Cakir, J. Suh, S. Tongay, Y. S. Huang, C. H. Ho, J. Wu, H. Sahin, and F. M. Peeters, Phys. Rev. B **89**, 155433 (2014).

[17] B. Chen, H. Sahin, A. Suslu, L. Ding, M. I. Bertoni, F. M. Peeters, and S. Tongay, ACS Nano **9**, 5326 (2015).

[18] M. Zhong, S. Zhang, L. Huang, J. You, Z. Wei, X. Liu, and J. Li, Nanoscale **9**, 3736 (2017).

[19] C. Vorwerk, C. Hartmann, C. Cocchi, G. Sadoughi, S. N. Habisreutinger, R. Félix, R. G. Wilks, H. J. Snaith, M. Bar, and C. Draxl, J. Phys. Chem. Lett. **9**, 1852 (2018).

[20] C. Vorwerk, C. Cocchi, and C. Draxl, Phys. Rev. B **95**, 155121 (2017).

[21] A. S. Toulouse, B. P. Isaacoff, G. Shi, M. Matuchova, E. Kioupakis, and R. Merlin, Phys. Rev. B **91**, 165308 (2015).

[22] M. Baibarac, N. Preda, L. Mihut, I. Baltog, S. Lefrant, and J. Mevellec, J. Phys.: Condens. Matter **16**, 2345 (2004).

[23] N. Preda, L. Mihut, M. Baibarac, I. Baltog, and S. Lefrant, J. Phys.: Condens. Matter **18**, 8899 (2006).

[24] J. Zhang, T. Song, Z. Zhang, K. Ding, F. Huang, and B. Sun, J. Mater. Chem. C **3**, 4402 (2015).

[25] X. Liu, S. T. Ha, Q. Zhang, M. de la Mata, C. Magen, J. Arbiol, T. C. Sum, and Q. Xiong, ACS Nano **9**, 687 (2015).

[26] A. Guloy, Z. Tang, P. Miranda, and V. Srdanov, Adv. Mater. **13**, 833 (2001).

[27] L. Cabana, B. Ballesteros, E. Batista, C. Magén, R. Arenal, J. Oró-Solé, R. Rurali, and G. Tobias, Adv. Mater. **26**, 2016 (2014).

[28] M. Zhou, W. Duan, Y. Chen, and A. Du, Nanoscale **7**, 15168 (2015).

[29] Y. Wang, Y.-Y. Sun, S. Zhang, T.-M. Lu, and J. Shi, Appl. Phys. Lett. **108**, 013105 (2016).

[30] C. V. Raman, Indian J. Phys. **2**, 387 (1928).

[31] A. C. Ferrari, J. C. Meyer, V. Scardaci, C. Casiraghi, M. Lazzeri, F. Mauri, S. Piscanec, D. Jiang, K. S. Novoselov, S. Roth, and A. K. Geim, Phys. Rev. Lett. **97**, 187401 (2006).

[32] X.-F. Qiao, X.-L. Li, X. Zhang, W. Shi, J.-B. Wu, T. Chen, and P.-H. Tan, Appl. Phys. Lett. **106**, 223102 (2015).

[33] X. Zhang, W. P. Han, J. B. Wu, S. Milana, Y. Lu, Q. Q. Li, A. C. Ferrari, and P. H. Tan, Phys. Rev. B **87**, 115413 (2013).

[34] P. H. Tan, W. P. Han, W. J. Zhao, Z. H. Wu, K. Chang, H. Wang, Y. F. Wang, N. Bonini, N. Marzari, N. Pugno, G. Savini, A. Lombardo, and A. C. Ferrari, Nat. Mater. **11**, 294 (2012).

[35] J.-B. Wu, X. Zhang, M. Ijas, W.-P. Han, X.-F. Qiao, X.-L. Li, D.-S. Jiang, A. C. Ferrari, and P.-H. Tan, Nat. Commun. **5**, 5309 (2014).

[36] J.-B. Wu, Z.-X. Hu, X. Zhang, W.-P. Han, Y. Lu, W. Shi, X.-F. Qiao, M. Ijias, S. Milana, W. Ji, A. C. Ferrari, and P.-H. Tan, ACS Nano **9**, 7440 (2015).

[37] Ph. Colomban, Spectrosc. Eur. **15**, 8 (2003).

[38] G. Gouadec and Ph. Colomban, Prog. Cryst. Growth Charact. Mater. **53**, 1 (2007).

[39] M. Havel, D. Baron, and Ph. Colomban, J. Mater. Sci. **39**, 6183 (2004).

[40] X. Zhang, X.-F. Qiao, W. Shi, J.-B. Wu, D.-S. Jiang, and P.-H. Tan, Chem. Soc. Rev. **44**, 2757 (2015).

[41] G. Kresse and J. Hafner, Phys. Rev. B **47**, 558 (1993).

[42] G. Kresse and J. Furthmuller, Phys. Rev. B **54**, 11169 (1996).

[43] J. P. Perdew, K. Burke, and M. Ernzerhof, Phys. Rev. Lett. **77**, 3865 (1996).

[44] S. J. Grimme, J. Comput. Chem. **27**, 1787 (2006).

[45] J. Heyd, G. E. Scuseria, and M. Ernzerhof, J. Chem. Phys. **118**, 8207 (2003).

[46] G. Henkelman, A. Arnaldsson, and H. Jónsson, Comput. Mater. Sci. **36**, 354 (2006).

[47] A. Fonari and S. Stauffer, https://github.com/raman-sc/VASP/ (2013).

[48] G. Placzek, U.C.R.L. Transl. 526 (L) **6**, 205 (1934).

[49] K. Momma and F. Izumi, J. Appl. Crystallogr. **41**, 653 (2008).

[50] C. Bacaksiz and H. Sahin, RSC Adv. **6**, 89708 (2016).

[51] D. J. Griffiths, *Introduction to Quantum Mechanics* (Pearson Prentice Hall, Englewood Cliffs, MA, 2005).

[52] A. Majumdar and D. Gerace, Phys. Rev. B **87**, 235319 (2014).

[53] A. N. Rudenko, S. Yuan, and M. I. Katsnelson, Phys. Rev. B **92**, 085419 (2015).

[54] V. N. Popov, Phys. Rev. B **67**, 085408 (2003).

[55] G. W. Ford and R. F. OConnell, Phys. Rev. B **75**, 134301 (2007).

[56] H. Li, Q. Zhang, C. C. R. Yap, B. K. Tay, T. H. T. Edwin, A. Olivier, and D. Baillargeat, Adv. Func. Mater. **22**, 1385 (2012).

[57] A. Berkdemir, H. R. Gutierrez, A. R. Botello-Mendez, N. Perea-Lopez, A. L. Elias, C.-I. Chia, B. Wang, V. H. Crespi, F. Lopez-Urias, J.-C. Charlier, H. Terrones, and M. Terronesa, Sci. Rep. **3**, 1755 (2013).

[58] K. H. Michel and B. Verberck, Phys. Rev. B **85**, 094303 (2012).

[59] C. H. Lui, L. M. Malard, S. H. Kim, G. Lantz, F. E. Laverge, R. Saito, and T. F. Heinz, Nano Lett. **12**, 5539 (2012).